



HAL
open science

Microstructure Evolution of Commercial Pure Titanium During Interrupted In Situ Tensile Test

Qian Wang, Shiyang Wang, Patrick Moll, Auriane Mandrelli, Jean-Sébastien
Lecomte, Christophe Schuman

► **To cite this version:**

Qian Wang, Shiyang Wang, Patrick Moll, Auriane Mandrelli, Jean-Sébastien Lecomte, et al.. Microstructure Evolution of Commercial Pure Titanium During Interrupted In Situ Tensile Test. Metallurgical and Materials Transactions A, 2021, 52, pp.2477 - 2488. 10.1007/s11661-021-06237-1 . hal-03863911

HAL Id: hal-03863911

<https://cnrs.hal.science/hal-03863911>

Submitted on 6 Dec 2022

HAL is a multi-disciplinary open access archive for the deposit and dissemination of scientific research documents, whether they are published or not. The documents may come from teaching and research institutions in France or abroad, or from public or private research centers.

L'archive ouverte pluridisciplinaire **HAL**, est destinée au dépôt et à la diffusion de documents scientifiques de niveau recherche, publiés ou non, émanant des établissements d'enseignement et de recherche français ou étrangers, des laboratoires publics ou privés.

Microstructure evolution of commercial pure titanium during interrupted in-situ tensile test

Qian Wang ^{a,b}, Shiyong Wang ^c, Patrick Moll ^{a,b}, Auriane Mandrelli ^{a,b}, Jean-Sébastien Lecomte ^{a,b,*}, Christophe Schuman ^{a,b,**}

^aLaboratoire d'Etude des Microstructures et de Mécanique des Matériaux (LEM3), Université de Lorraine, CNRS, Arts et Métiers ParisTech, Metz 57073, France

^bLaboratory of Excellence on Design of Alloy Metals for low-mAss Structures (DAMAS), Université de Lorraine, Metz 57073, France

^cSchool of Materials Science & Engineering, Changzhou University, Changzhou, Jiangsu 213164, China

*Corresponding author.

**Corresponding author.

E-mail addresses: jean-sebastien.lecomte@univ-lorraine.fr

christophe.schuman@univ-lorraine.fr

1 Abstract

2 Microstructure evolution of commercial pure titanium is investigated by interrupted in-situ
3 electron backscatter diffraction (EBSD) measurement during tensile deformation along
4 transverse direction at room temperature. After 24% elongation, the split basal texture of initial
5 material is weakened and rotated around 90° along normal direction (**ND**). $\{11\bar{2}2\}$ - $\{10\bar{1}2\}$
6 double twin is the main reason for the change of texture. The basal poles are rotated nearly
7 perpendicular to **ND** by the primary $\{11\bar{2}2\}$ twin and back to **ND** through the reorientation of
8 $\{10\bar{1}2\}$ secondary twin. Both Schmid factor criterion and displacement gradient
9 accommodation are considered to predict the twin-induced texture evolution during **TD** tension.
10 Kink bands formed by the accumulation of basal $\langle a \rangle$ dislocations are also observed in the
11 deformed grain. The activation of other slip systems can deviate the rotation axis and reduce
12 the rotation angle of kink boundary. Besides, the kink boundary with high basal dislocation
13 density obviously hinder the twin transmission and simultaneously can be taken as a preferential
14 nucleation site for $\{11\bar{2}2\}$ twin.

15 **Keywords:** Titanium; Tension; Texture; $\{11\bar{2}2\}$ twin; $\{10\bar{1}2\}$ twin; Kink band;

16 **1. Introduction**

17 Commercially pure titanium (CP-Ti) sheets have widely been used in chemical plants,
18 consumer products, and heat exchangers [1,2], due to its high strength, corrosion resistance,
19 burning resistance, and biological compatibility. Rolled α -Ti plate generally has a split-basal
20 texture with the c -axis of the hexagonal close-packed (HCP) lattice inclined at an angle of 20° –
21 40° from the normal direction (**ND**) of the rolling plane towards the transverse direction (**TD**)
22 [3]. Such a specific crystallographic feature introduces a severe anisotropy in deformation
23 characteristics [4,5], mechanical properties [6] and formability [7], which is much more
24 pronounced than that of other sheet metals such as steel and aluminum alloys. For this reason,
25 understanding related mechanisms of deformation anisotropy in rolled α -Ti plate is an essential
26 prerequisite.

27 The common plastic deformation modes in CP-Ti are slip (prismatic slip) and twinning
28 ($\{10\bar{1}2\}$ extension and $\{11\bar{2}2\}$ contraction twinning). The ease of slip or twinning on a
29 particular system is quantified by the critical resolved shear stress (CRSS). The relative
30 activities of twinning and slip are also significantly dependent on the loading direction due to
31 the strong rolling texture of as-received sample and the directional nature of deformation modes
32 [8]. Dynamic compressive tests were carried out along **ND** in [9], maximum basal pole intensity
33 was reoriented toward **ND** at the 40% thickness reduction. Apart from $\{11\bar{2}2\}$ - $\{10\bar{1}2\}$ double
34 twins, the accumulation of $\langle a \rangle$ and pyramidal $\langle c+a \rangle$ slips also gave rise to the strong basal
35 texture. By conducting uniaxial compression along rolling direction (**RD**) and **ND**, Woo et al.
36 [10] proposed that the primary and secondary twins are the main reason for the anisotropic
37 texture evolution and Schmid factor (SF) criterion is a major mechanism controlling overall
38 twinning characteristics. However, SF criterion is debatable for predicting general twin variant
39 activation, the local stresses inside a grain could differ from the externally applied stress state,
40 only 45%-50% of the cases are correct for the condition of rolling [11]. Displacement gradient
41 accommodation (DGA) can more correctly predict the selection of secondary twin variants [12],
42 and should also be considered on controlling the twin-induced texture evolution.

43 Compared with slip and twinning, “deformation kinking” is a less common deformation
44 mode, but it is considered important for materials that exhibit strong plastic anisotropy, such as
45 Zn [13,14], Mg/LPSO two-phase alloys [15,16], where LPSO phase is a long-period stacking
46 ordered phase in Mg alloy. Hess and Barrett [13] first proposed a dislocation-based model to
47 explain kink band formation. In this model, cooperative operation followed by arrangement of
48 basal dislocations to align perpendicular to the slip plane were believed to be the basic process

49 to form the deformation kink boundary. For HCP phase, the deformation kink band boundary
50 was mainly constructed by the array of basal dislocations [14,17]. Besides, it is discovered
51 recently that kink band is an effective deformation mode to accommodate the plastic strain in
52 LPSO phase [18]. In LPSO phase, the kink band can be classified into three types according to
53 Taylor axes of slips: $\langle 1\bar{1}00 \rangle$ or $\langle 0\bar{1}10 \rangle$ rotation type, $\langle 0001 \rangle$ rotation type and $\langle 1\bar{2}10 \rangle$
54 rotation type, which are produced by basal $\langle a \rangle$ slip, prismatic $\langle a \rangle$ slip and a combination of
55 two basal slip variants, respectively. Furthermore, some researchers have argued that $\{11\bar{2}1\}$
56 twin can be regarded as “geometry-fixed deformation kink band” [19]. Jin et al. [17] proposed that
57 $\{11\bar{2}1\}$ twin is formed by a gradual evolution from kink band through accumulative basal
58 dislocation slips. However, the research on kinking deformation was rather limited in titanium
59 alloys [17,20], because they undergo twinning as an accommodation mechanism against stress
60 concentration.

61 In the present work, the microstructure of CP-Ti was observed by interrupted in-situ electron
62 backscatter diffraction (EBSD) measurements during tensile tests at room temperature. The
63 paper is structured as follows. Section 2 gives a description of the sample preparation for
64 interrupted in-situ experiment and EBSD characterization. Section 3 presents the texture
65 component after large deformation resulting from different twin modes and characters of the
66 double twins and kink bands are introduced individually in detail. In section 4, the basal texture
67 change induced by $\{11\bar{2}2\}$ - $\{10\bar{1}2\}$ double twin during **TD** tension is predicted by the
68 combination of SF and DGA criterions.

69 **2. Methodology**

70 **2.1 Experimental process**

71 The material used in this work is rolled commercially pure titanium T40 (ASTM grade 2)
72 sheet with the thickness of 1 mm. The sheet was annealed at 750 °C for 1 h to obtain a fully
73 recrystallized microstructure. The tensile specimens were cut by electrical discharge wire-
74 cutting and the gauge dimensions are shown in Fig. 1a. The loading direction was chosen to be
75 parallel to **TD** of titanium plate. According to the work of Wronski et al. [21], a titanium T40
76 alloy plate was tested, the results showed that twins appeared frequently in the sample elongated
77 along **TD** in contrast to the **RD** tensile sample.

78 The sample preparation and interrupted in-situ experiment generally followed the method
79 of Wang et al. [22]. Sample surface was treated for orientation detection before loading, enough
80 indexation rate (> 90%) can also be obtained with increased deformation amount. Interrupted

81 in-situ tension was performed step by step in the tensile machine MT100 as illustrated in Fig.
82 1b under the tensile speed of 150 $\mu\text{m}/\text{min}$. To follow the microstructure evolution of the same
83 zone under EBSD measurement, the zone of interest at the center of tensile sample was marked
84 by micro-indentation. After each step of tensile deformation, the sample was unloaded to
85 calculate the engineering strain (respective 8%, 16%, and 24%) and then crystallographic
86 characterization was performed.

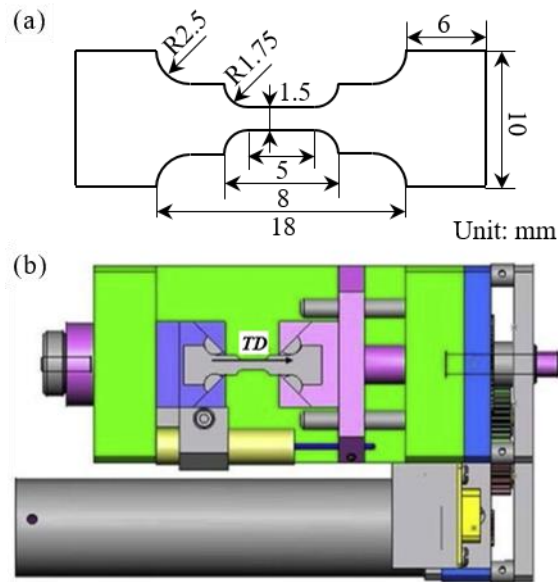


Fig. 1. (a) Tension sample dimension with thickness of 1 mm. (b) Sketch of the tension machine.

87 Before EBSD characterization, the sample was ground with SiC papers of grits from 1200[#]
88 to 2400[#], followed by electrolytic polishing using a solution of 10 vol% perchloric acid in
89 methanol at 35 V and 5 °C for 5 s. The characterization was performed using JSM 6490
90 scanning electron microscopy equipped with an EBSD camera with a specimen tilt of 70°, an
91 accelerating voltage of 15 kV, a working distance of 15 mm and a step size of 1.5 μm . Four
92 separate EBSD maps were obtained at the marked zone of the specimen to cover enough grains
93 (around 84) and merged into one large image by Oxford-HKL channel 5 post-analysis software.
94 Texture evolution was analyzed by ATEX software [23]. The geometrically necessary
95 dislocation (GND) density was also calculated by ATEX software [23] according to the method
96 described in literature [24].

97 2.2 Crystallography of twin and kink band

98 During deformation, the participation of twinning is required in titanium due to the limited
99 slip systems. In the classical theory of deformation twinning, the parent lattice is reoriented by

100 atom displacements (\mathbf{u}) which are equivalent to a simple shear of the lattice points. The
 101 twinning displacement in the twinning frame is shown in Fig. 2. The twinning frame is set up
 102 by: \mathbf{n} // twinning shear direction, \mathbf{m} // normal of twin habit plane and \mathbf{p} // normal of shear plane.
 103 The displacement gradient tensor of twinning (\mathbf{D}^t) has a simple form in the twinning frame [25]:

$$\mathbf{D}^t = \frac{\partial u_i}{\partial Z_i} = \begin{bmatrix} 0 & 0 & s \\ 0 & 0 & 0 \\ 0 & 0 & 0 \end{bmatrix} \quad (1)$$

104 where \mathbf{u} is displacement vector at position Z_i ($i = 1 \dots 3$) and s is the magnitude of twinning
 105 shear in Ti ($c/a=1.587$). The s values of $\{10\bar{1}2\}$ and $\{11\bar{2}2\}$ twins in titanium are 0.173 and
 106 0.218, respectively. The orientation of the twin lattice can also be produced directly by a
 107 reflection of parent lattice in the twin habit plane or a 180° rotation about shear direction. Due
 108 to the crystal symmetry, the misorientations of $\{10\bar{1}2\}$ and $\{11\bar{2}2\}$ twins are $85^\circ/\langle 11\bar{2}0 \rangle$ and
 109 $64^\circ/\langle 10\bar{1}0 \rangle$, respectively.

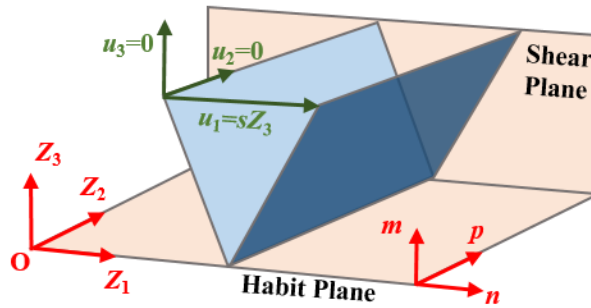


Fig. 2. Schematic diagram of twinning

110 The model for kinking mechanism in HCP crystal is firstly proposed by Hess and Barrett
 111 for a Zn single crystal [13], as shown in Fig. 3a. Kinking occurs by progressive lattice rotation
 112 within the band due to the accumulated basal slips perpendicular to slip plane as plastic
 113 deformation proceeds. It is different from twinning formed by abrupt shear into the final
 114 orientation, but it can be regarded as a origin of $\{11\bar{2}1\}$ twin nucleation [17]. To obtain a valuable
 115 geometric information, the lattice rotation axis and rotation angle $\Delta\phi$ were used to describe an
 116 individual kink band (Fig. 3b). The rotation axis can be determined through intragranular
 117 misorientation axis (IGMA) analysis [18,26] by matching the Taylor axis of a known slip mode.
 118 The Taylor axes of different slip systems in titanium are shown in Table 1. The kink band in
 119 HCP material is usually induced by basal slip [14,17], the misorientation axis is focus on $\langle 10\bar{1}0 \rangle$.
 120 There appear three types of kink bands corresponding to three variants of basal slip, as shown
 121 in Table 2. The askew rotation axis from Taylor axis $\langle 10\bar{1}0 \rangle$ can be induced by the other slip

122 systems activated near the kink band. The rotation angle $\Delta\phi$ is between the basal plane of kink
 123 band and matrix, which is related to the dislocation density and the dislocation wall thickness
 124 [18]. The habit plane $\{1\bar{2}1k\}$ of each type kink band is rotated from $\{1\bar{2}10\}$ around $\langle 10\bar{1}0 \rangle$ axis
 125 and the value k varies with the rotation angle $\Delta\phi$. The angle between $\{1\bar{2}10\}$ and $\{1\bar{2}1k\}$ is
 126 equals to the $\Delta\phi/2$.

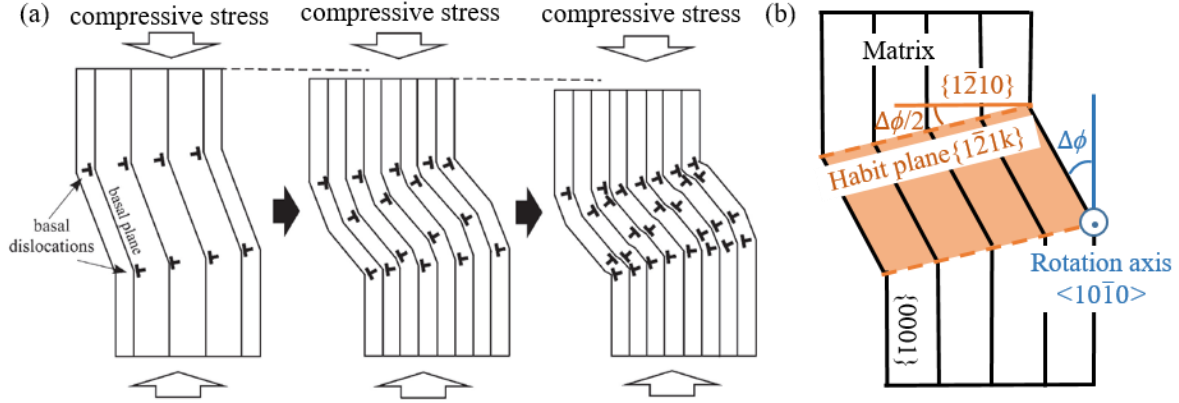


Fig. 3. (a) Model of deformation kink band formed in the Zn single crystal (reprinted from [13]). (b) Schematic on crystal rotation angle (misorientation angle) and crystal rotation axis of kink band.

127 3. Results

128 3.1 Twinning induced texture evolution

129 Fig. 4a-d show the microstructures of initial sample and the material stretched along **TD** to
 130 8%, 16% and 24%, where **ND** axis was projected with the shown color bar. The as-received
 131 material has already fully recrystallized with the average grain size of around 100 μm . With the
 132 increase of elongation, there appear more and more twinning operations, which significantly
 133 change the grain orientations.

134 Besides, the intragranular orientation change indicates the existence of GNDs after
 135 deformation. GNDs are created to accommodate the lattice curvature, the distribution of which
 136 can be measured with misorientation data from conventional Hough-based EBSD technique [24].
 137 The Nye dislocation density tensor (α_{ij}) [24] is a sum over individual dislocation densities ρ^t of
 138 different dislocation types (t), each characterized by Burgers vector \mathbf{b}^t and line vector \mathbf{l}^t ,

$$\alpha_{ij} = \sum_{t=1}^N b_i^t l_j^t \rho^t \quad (2)$$

139 GND norm is the entrywise norm of the Nye Tensor [23],

$$\|\alpha\| = \sqrt{\alpha_{ij}\alpha_{ij}} \quad (3)$$

140 The average GND norms of initial and strained samples are measured by corresponding EBSD
 141 maps Fig. 4a-d. The results are presented in Fig. 5. Compared to the initial sample, the average
 142 GND norm is nearly unchanged after 8% strain and slightly increase in 16% tensile sample.
 143 The high GND density of $1.9 \times 10^{-2} \mu\text{m}^{-1}$ after 24% tension shows that a huge amount of slip
 144 systems has been activated. Indeed, at large deformation, apart from twin, $\langle a \rangle$ and pyramidal
 145 $\langle c+a \rangle$ slips also gave rise to the texture evolution in pure titanium [9].

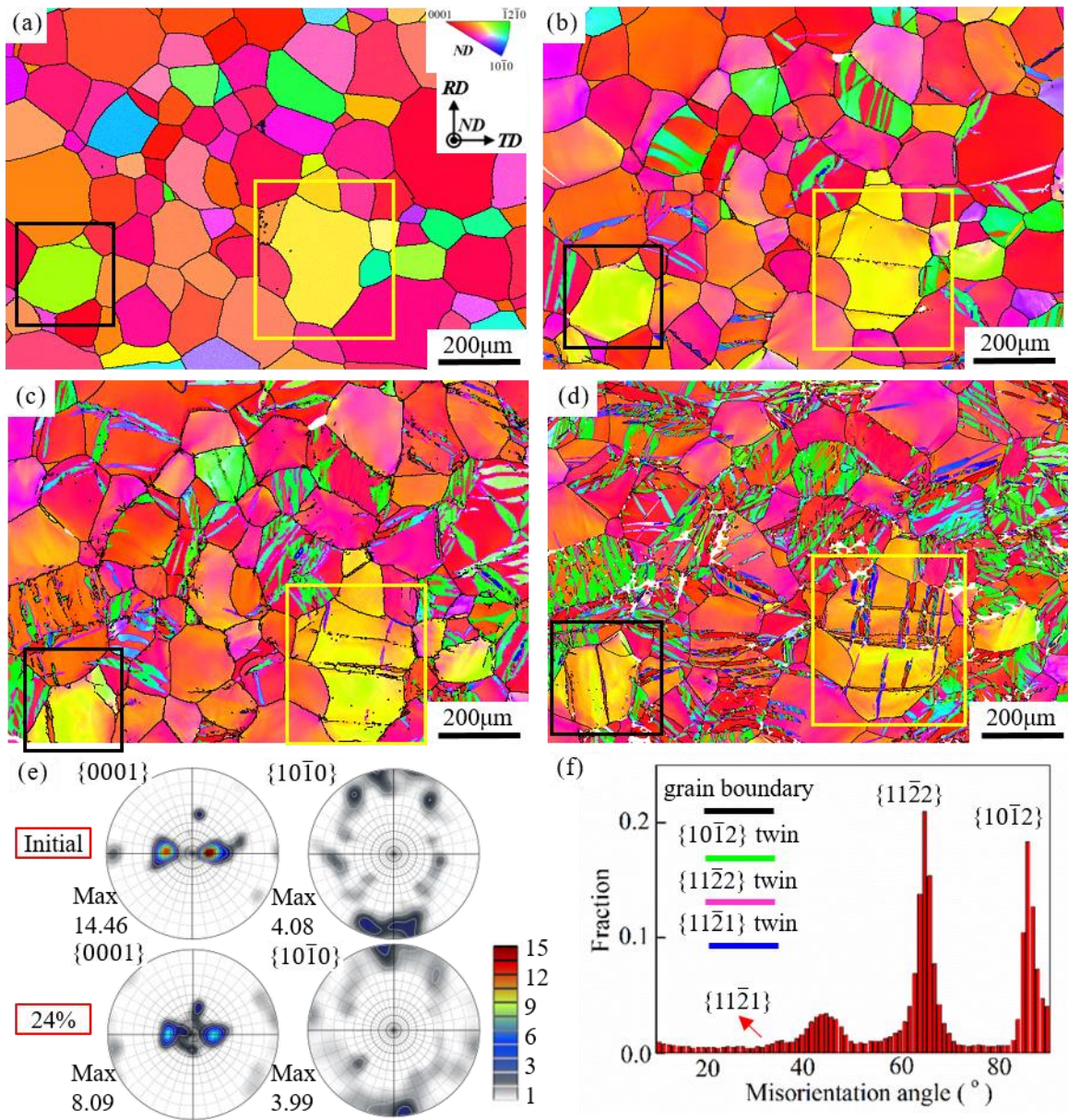


Fig. 4. Inverse pole figure (IPF) map of (a) initial microstructure (b) 8% (c) 16% (d) 24%. (e) Pole figures of $\{0001\}$ and $\{10\bar{1}0\}$ planes before and after 24% tension. (f) The corresponding misorientation angle distribution of 24% deformed sample.

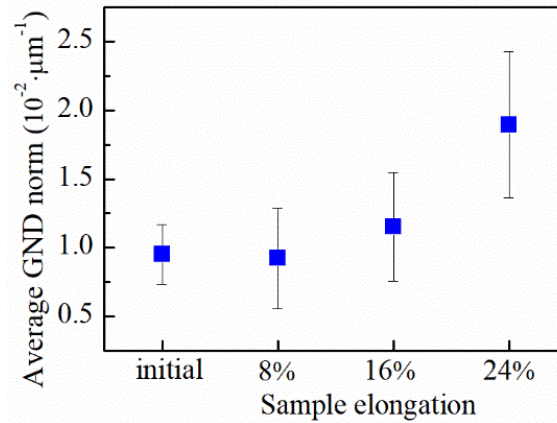


Fig. 5. The variation of average GND norms. Error bars are \pm one standard deviation which incorporates multiple measurements in the same sample.

146 The texture evolution during tensile loading is illustrated in Fig. 4e. The initial material
 147 exhibits a typical split basal texture with c -axes inclined $\pm 30^\circ$ from **ND** to **TD**. After 24%
 148 elongation, the initial split basal texture was weakened and partial c -axes trend to be rotated 90°
 149 around **ND**. Fig. 4f shows the histogram of misorientation distribution for the grain boundaries.
 150 Two significant peaks can be seen around 65° and 87° , which are attributed to the formation of
 151 $\{10\bar{1}2\}$ and $\{11\bar{2}2\}$ twin, respectively. Thus, the activation of $\{10\bar{1}2\}$ and $\{11\bar{2}2\}$ twin is the
 152 fundamental reason for the texture evolution during tensile test. $\{11\bar{2}1\}$ twin corresponds to the
 153 slight peak around 35° . A special peak between 40° and 50° arises from $\{11\bar{2}2\}$ - $\{10\bar{1}2\}$ double
 154 twins, which has been investigated in-depth by Xu et al. [27]. The most frequent misorientation
 155 between the $\{10\bar{1}2\}$ secondary twin and titanium matrix is 48.44° around $\langle\bar{5}503\rangle$, which is
 156 consistent with our experimental results.

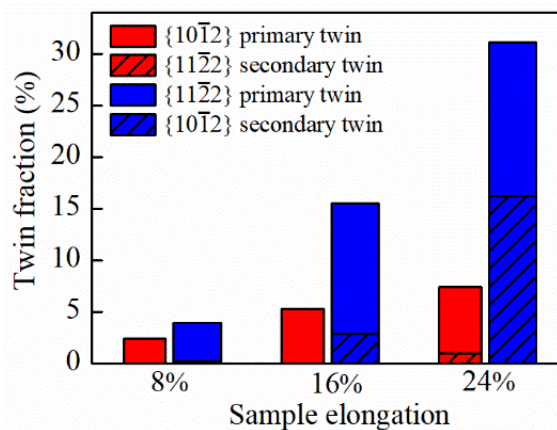


Fig. 6. Twin fraction in the sample with different elongations.

157 To calculate the twin area proportion, all the primary and secondary $\{10\bar{1}2\}$ and $\{11\bar{2}2\}$
158 twin grains formed in the observed 84 grains are manually picked out from the EBSD maps
159 (Fig. 4b-d). The results are shown by bar chart in Fig. 6. For each strained sample, the area
160 fractions of primary $\{10\bar{1}2\}$ (red) and $\{11\bar{2}2\}$ (blue) twin are separately drawn with two bars,
161 inside which the corresponding $\{11\bar{2}2\}$ and $\{10\bar{1}2\}$ secondary twin fraction are filled with
162 diagonal stripes. In the 8% elongation sample, the fractions of $\{10\bar{1}2\}$ and $\{11\bar{2}2\}$ twin are low,
163 respective 2.5% and 3.7%, and nearly no secondary twins are observed. After 16% tension, the
164 fraction of $\{11\bar{2}2\}$ twin (blue) around 15.5% increases rapidly and is three times the $\{10\bar{1}2\}$
165 twin (5.3%). Besides, a small amount of $\{11\bar{2}2\}$ - $\{10\bar{1}2\}$ double twins have been formed inside
166 primary $\{11\bar{2}2\}$ twin grains. Compared with primary $\{11\bar{2}2\}$ twin, the increase of primary
167 $\{10\bar{1}2\}$ twin fraction is relatively slight, indicating that **TD** tension is more favorable for
168 $\{11\bar{2}2\}$ twin. Although the CRSS value of $\{11\bar{2}2\}$ twin is higher than $\{10\bar{1}2\}$ twin in CP-Ti at
169 room temperature [28], the actual stimulation of twin system [28] is governed by the combination of
170 the SF and CRSS (i.e., activation stress = CRSS/SF). The $\{10\bar{1}2\}$ and $\{11\bar{2}2\}$ twin prefer to be
171 activated when *c*-axes are under tension and compression, respectively. Due to the basal texture
172 of titanium sample (basal poles // **ND**), *c*-axes are always compressed during **TD** tension and
173 the formation of $\{10\bar{1}2\}$ twin is restrained. Thus, when tensile strain proceeds to 24%, the
174 primary $\{10\bar{1}2\}$ twin fraction is almost unchanged and only a few secondary $\{11\bar{2}2\}$ twin occur.
175 Noting that the primary $\{11\bar{2}2\}$ twin fraction (31.1%) is twice that of 16% elongation sample
176 and half of the primary $\{11\bar{2}2\}$ twins are reoriented into secondary $\{10\bar{1}2\}$ twins to further
177 accommodate the external tensile strain. Therefore, forming large amount of primary $\{11\bar{2}2\}$
178 and secondary $\{10\bar{1}2\}$ twins is the main reason for the texture change during **TD** tension.

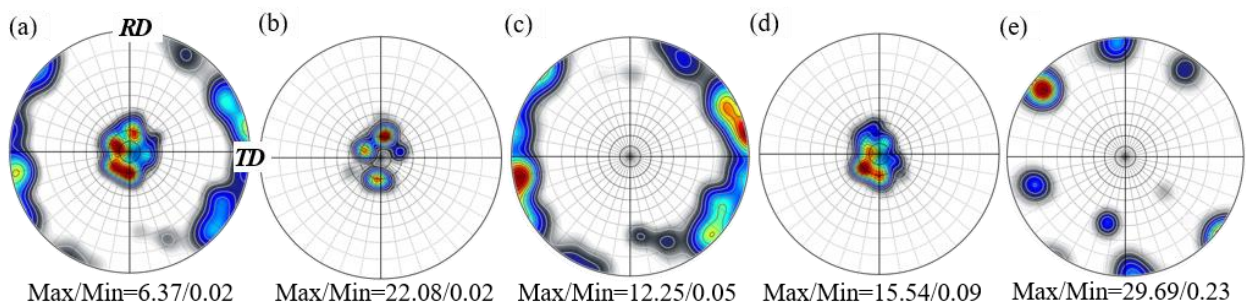


Fig. 7. $\{0001\}$ pole figures of deformation twins (a) All the deformation twins. (b) Primary $\{10\bar{1}2\}$ twins. (c) Primary $\{11\bar{2}2\}$ twins. (d) Secondary $\{10\bar{1}2\}$ twins. (e) Secondary $\{11\bar{2}2\}$ twins.

179 The texture of twin formed in 24% elongation sample is calculated to investigate the specific
 180 orientation change induced by each type of twin during tensile deformation. The {0001} pole
 181 figures of different deformation twins are presented in Fig. 7. Fig. 7a shows the texture of all
 182 the deformation twins, the strong {0001} poles are focus along **ND**. There also appear some
 183 weak peaks around **TD**. These different peaks show the different effect of twins on texture
 184 evolution during deformation. According to the {0001} pole figure of each type twin (see Fig.
 185 7b-e), the textures of primary and secondary {10 $\bar{1}2$ } twin are similar focus on the center of pole
 186 figures and the textures of {11 $\bar{2}2$ } twins are in **RD-TD** plane and close to **TD**. According to
 187 Fig. 6 the primary {11 $\bar{2}2$ } and secondary {10 $\bar{1}2$ } twins are dominant after 24% elongation. It
 188 can be derived that, under continuous tensile loading, the basal poles of as-received grains with
 189 basal texture are rotated into **RD-TD** plane by the formation of primary {11 $\bar{2}2$ } twins, and then
 190 oriented back to **ND** after significant activation of secondary {10 $\bar{1}2$ } twins.

191 The SF criterion is conveniently used as a reference for twin variant selection. It is based on
 192 the idealized hypothesis that the stress direction in individual grain is exactly the same as the
 193 nominal applied stress. Under uniaxial tension along **TD**,

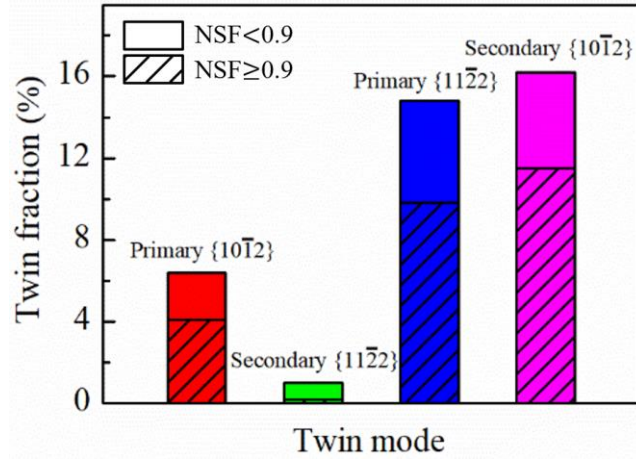
$$SF = \cos(\theta)\cos(\lambda) \quad (4)$$

194 where θ is the angle between twinning plane normal and loading direction, and λ is the angle
 195 between shear direction and loading direction. Normalized Schmid factor (NSF) was calculated
 196 to compare the SF of activated twin variant with the other possible variants in the same grain
 197 [27].

$$NSF(i) = SF(i) / SF_{\max}, i = 1 \dots 6 \quad (5)$$

198 The maximum possible value of $NSF(i)$ is 1. In the present work, the NSF's of all the primary
 199 and secondary {10 $\bar{1}2$ } and {11 $\bar{2}2$ } twin in Fig. 4d (24% strain) are measured as shown in Fig.
 200 8. The area fraction of each twin mode is the same as the value in Fig. 6. The twin variants with
 201 actually high SFs are defined as $NSF \geq 0.9$ filled with diagonal stripes. For the primary {10 $\bar{1}2$ }
 202 (red), secondary {11 $\bar{2}2$ } (green), primary {11 $\bar{2}2$ } (blue) and secondary {10 $\bar{1}2$ } (pink) twin, the
 203 high SF twin fractions ($NSF \geq 0.9$) are respective 64.1%, 16.1%, 66.5% and 70.8%. The
 204 abnormally low fraction 16.1% is controversial due to that the activated secondary {11 $\bar{2}2$ } twin
 205 is very few and insufficient for statistical analysis. The high SF twin fractions for the other three
 206 twin modes are relatively higher, showing that the variants with high SFs tend to be more active.
 207 According to Fig. 7, the oriented basal texture during tensile deformation is mainly depends on
 208 the primary {11 $\bar{2}2$ } and secondary {10 $\bar{1}2$ } twins, which always respects SF rule. The variant

209 selection induced by local strain accommodation and the prediction of tensile texture evolution
 210 will be further discussed in Section 4.



211
 212
 213 **Fig. 8.** Area fraction of twins as a function of the normalized Schmid factor
 214

215 3.2 Double twin and grain boundary sliding

216 The interrupted in-situ microstructures of four typical grains are shown in Fig. 9. The
 217 orientations of G1 and G2 are favorable for primary {10 $\bar{1}2$ } tension and {11 $\bar{2}2$ } compression
 218 twin, respectively, followed by the formation of secondary {11 $\bar{2}2$ } and {10 $\bar{1}2$ } twin during
 219 continuous deformation. Six {10 $\bar{1}2$ } and {11 $\bar{2}2$ } twin variants are denoted by respective T_i and
 220 C_i ($i = 1,2,3\dots6$). In order to facilitate analysis, the twin variants of double twin are presented
 221 in the crystal frame of primary twin. Six twin variants of each twin system are given by their
 222 corresponding twin planes and shear directions, as shown in Table 3.

223 G1 has the orientation favorable for {11 $\bar{2}2$ } twin. Two primary {11 $\bar{2}2$ } twin variants are
 224 observed after 16% elongation, C_5 (SF: 0.42) and C_4 (SF: 0.15). In Fig. 9c and d, the size of C_4
 225 variant with lower SF is larger than C_5 . It is considered that variants achieving certain pertinent
 226 local strain accommodations in their neighborhoods can be preferentially activated [29]. Twins
 227 accommodated by the twins in neighboring grain have a great capacity to develop into large
 228 size [22]. Indeed, there appears adjoined twin to active large C_4 in the upside neighboring grain
 229 (G5), the accommodation mechanism can be found in discussion. After 24% elongation,
 230 secondary {10 $\bar{1}2$ } twins nearly cover the C_4 and C_5 twin. The formed double twins are C_4 - T_5
 231 and C_5 - T_5 . The variant selection of {11 $\bar{2}2$ } - {10 $\bar{1}2$ } double twin in CP-Ti under ND
 232 compression were explored in [30]. By the method of displacement gradient accommodation
 233 (DGA) criterion, they suggested that the C_i - T_i/T_{i+1} double twins are the most predominant

234 because the T_i/T_{i+1} variants have the highest capacity to accommodate the primary C_i twin. The
 235 other types of double twins are less. Indeed, the dominant double twin in G1 are C_4 - T_5 and C_5 -
 236 T_5 . The variant selection of $\{11\bar{2}2\}$ - $\{10\bar{1}2\}$ double twin between T_i and T_{i+1} will be further
 237 discussed in Section 4.

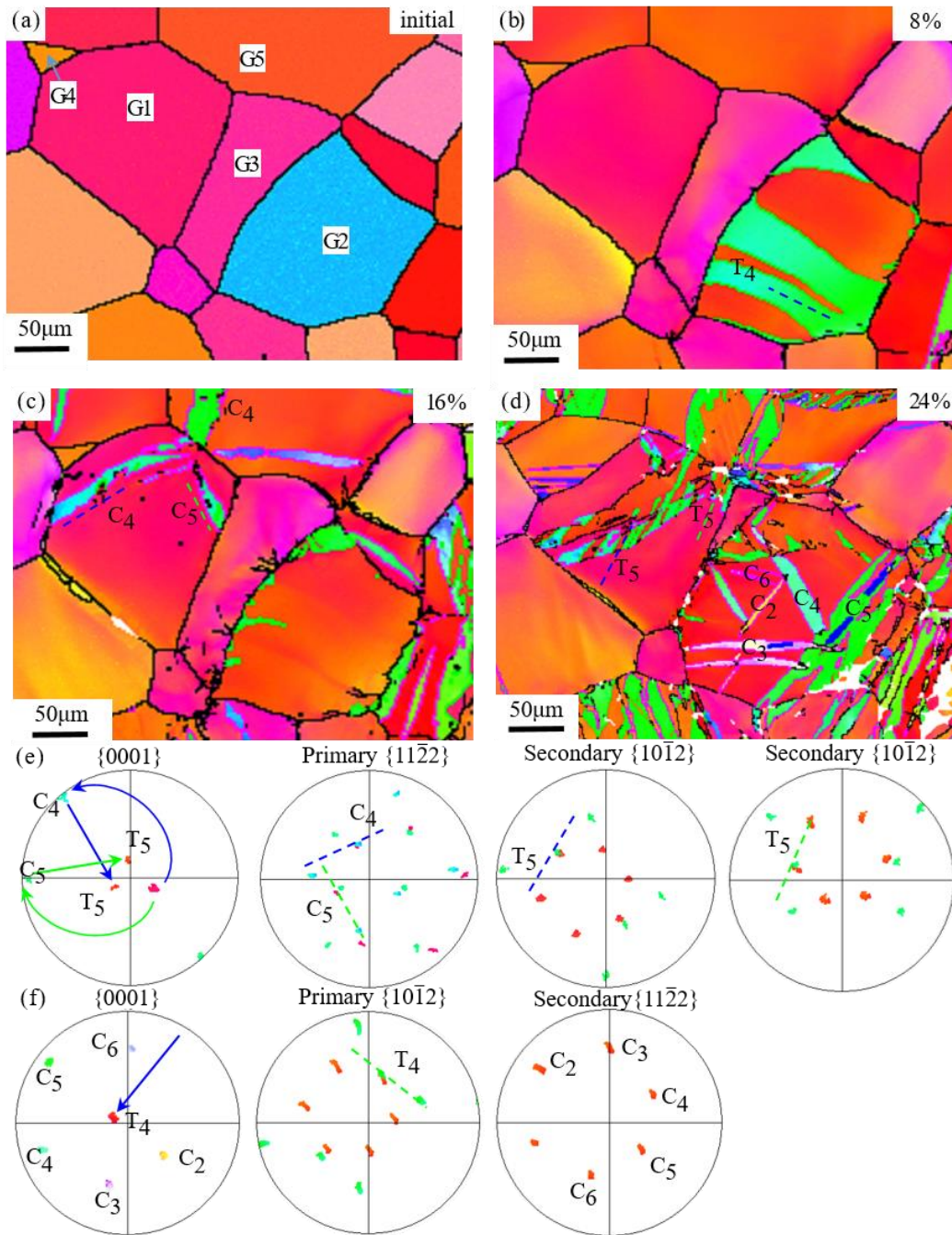


Fig. 9. The interrupted in-situ microstructures of four typical grains (G1-G4) during tension (a) initial (b) 8 % (c) 16 % (d) 24 %. (e) pole figures of $\{11\bar{2}2\}$ - $\{10\bar{1}2\}$ double twins in G1 (f) pole figures of $\{10\bar{1}2\}$ - $\{11\bar{2}2\}$ double twins in G2. The color of dots in pole figures is corresponding to IPF color. The dotted lines show the traces of primary and secondary twin planes. (Euler angles of G1: 75.7° , 28.6° , 24.9° ; G2: 146.2° , 87.5° , 17.1° ; G3: 97.0° , 142.5° , 36.0° and G4: 77.7° , 148.8° , 58.3°)

238 The orientation of G2 is favorable for the primary $\{10\bar{1}2\}$ twin. The $\{10\bar{1}2\}$ twin T₄ with
239 largest SF (0.14) can be easily formed after a small elongation of 8% (see Fig. 9b). Different
240 from the lenticular microscopy of primary $\{11\bar{2}2\}$ twin in G1, the primary $\{10\bar{1}2\}$ twin can
241 quickly grow up and cover the whole grain after 16% elongation in Fig. 9c. The easy growth of
242 $\{10\bar{1}2\}$ twin can be due to the lower twin shear than $\{11\bar{2}2\}$ twin. After 24% elongation, five
243 secondary $\{11\bar{2}2\}$ variants are activated in T₄. There is not obvious variant selection for
244 $\{10\bar{1}2\}$ - $\{11\bar{2}2\}$ double twin in this work. The stimulation of these different secondary $\{11\bar{2}2\}$
245 twin variants is likely due to the complicated internal stress in primary $\{10\bar{1}2\}$ twin.

246 Furthermore, significant grain boundary sliding is observed in G3 and G4 during tensile
247 deformation. With the increase of elongation, the accumulated heterogeneous deformation
248 along grain boundaries produced by the accumulation of dislocations and/or twin shear,
249 leads to orientation gradients exceeding 10° over 10–20 μm. At large strain, several slip
250 systems, prism $\langle a \rangle$, basal $\langle a \rangle$ and pyramidal $\langle c+a \rangle$ slips operate within grains and
251 maintain strain compatibility requirements [9]. Grain boundary sliding can be induced by
252 the accumulated dislocations to reduce the grain size of G3 and relax the local plastic
253 anisotropy and deformation heterogeneities. As for G4, the orientation is favorable for
254 $\{11\bar{2}2\}$ twin, but the grain size is small. It is well recognized that large grains facilitate the
255 activity of deformation twin [31]. In the 24% strained sample, the twins in the fine grain
256 with soft orientation are also stimulated to accommodate the larger external strain. And
257 then, the grain boundaries expand outward to relax the twin shear and accelerate the twin
258 growth, which finally leads to the increase of grain size of G4.

259 3.3 Kink band

260 Besides twinning and slip, deformation kinking also takes place in the tensile sample. The
261 details of kink bands and their interactions with twin and slip are presented in Fig. 10 and Fig.
262 11. In Fig. 10a, two parallel kink bands are formed in G6 during deformation. According to
263 Table 2 and the $\langle 10\bar{1}0 \rangle$ pole figures in Fig. 10d and e, the rotation axis of the two kink bands
264 is $[1\bar{1}00]$. Thus, they belong to K₁ variant and are denoted by K_{1L} (left) and K_{1R} (right). Their
265 habit planes are respective $(11\bar{2}1)$ and $(\bar{1}\bar{1}2\ 0.5)$ as shown by the pole figures in Fig. 10d and e.
266 According to the interrupted in-situ microstructures of G6 in Fig. 4a-d, in the black box at
267 bottom left, K_{1L} is formed first at 16% strained sample, while K_{1R} is formed afterwards with
268 further deformation. In Fig. 10a, K_{1L} is much thicker than K_{1R} indicating that the formed kink
269 band can get thickened with increased deformation.

270 The average of the misorientation angle is measured by the values at randomly selected ten
 271 positions along kink band boundary. The average misorientation value for K_{IL} in 16%
 272 elongation sample is around 25.9° , which decrease to 12.5° after 24% elongation. Similarly,
 273 with the increase of strain, the average misorientation for K_{IR} around 27.2° will also decrease
 274 with further deformation. The reduced rotation angle of kink band means the decrease of basal
 275 dislocation density [18]. The IGMA distributions in Fig. 10b and c are drawn to show the
 276 different misorientation distributions of K_{IL} and K_{IR} . In 24% tensile sample, misorientation
 277 angles of K_{IR} are focused around $\langle 10\bar{1}0 \rangle$ axis, while the distribution of K_{IR} is discrete from
 278 $\langle 10\bar{1}0 \rangle$ axis to $\langle 0001 \rangle$ axis. $\langle 10\bar{1}0 \rangle$ and $\langle 0001 \rangle$ axis are Taylor axes of basal and prismatic
 279 $\langle a \rangle$ slip, respectively (Table 1). Therefore, the accumulated basal dislocations at kink band
 280 boundary can be transformed into prismatic dislocations or glide away during continuous
 281 deformation.

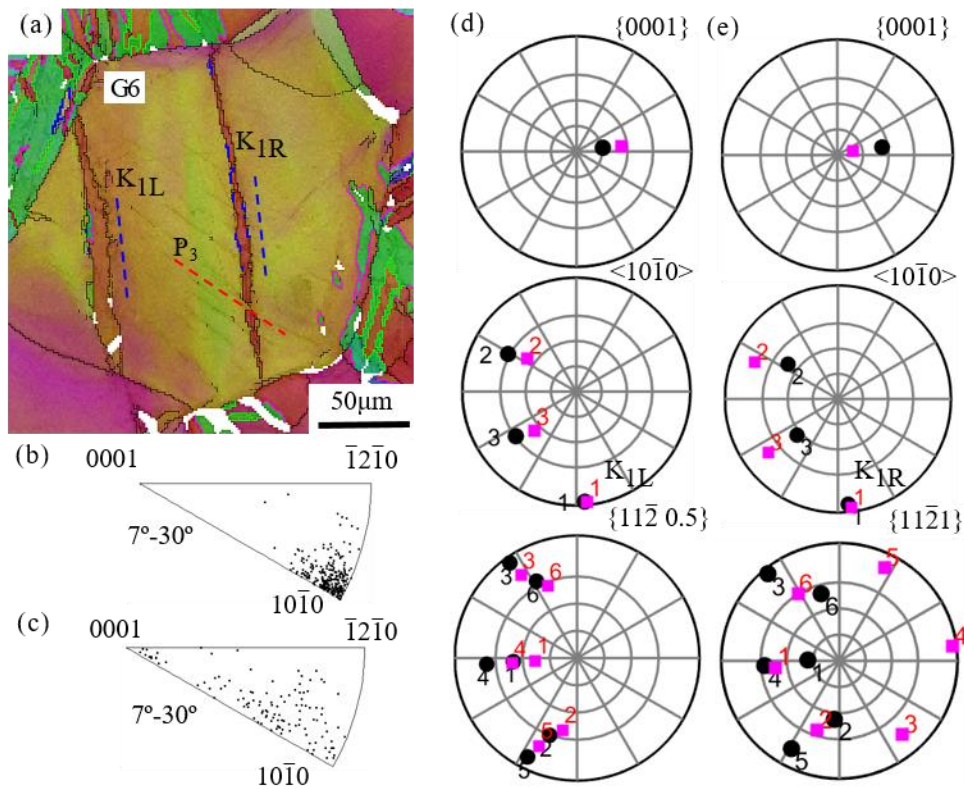


Fig. 10. (a) IPF map of G6 with kink band after 24% elongation. (b) and (c) IGMA distributions around kink band boundary of respective K_{IR} and K_{IL} obtained from misorientation angles of 7° - 30° . (d) and (e) Pole figures of K_{IL} and K_{IR} , respectively. In pole figures, the pink and black dots represent the direction or plane in respective kink band and matrix. The dotted lines show the traces of kink band habit plane or slip plane. (Euler angle of matrix: 100.4° , 41.4° , 54.5°)

282 Noting that some segments of K_{IR} are identified as $\{11\bar{2}1\}$ twin boundary ($35^\circ/\langle 10\bar{1}0 \rangle$).
283 However, no $\{11\bar{2}1\}$ twin occur in K_{IL} showing that the twin segments can be formed at initial
284 nucleation of kink band (K_{IR}) at 16% strain which are not stable in G6 and will disappear during
285 further deformation. Jin et al. ^[17] proposed the formation mechanism of $\{11\bar{2}1\}$ twin through
286 kinking in titanium. The $\{11\bar{2}1\}$ twin formed by kinking mechanism mainly occurs in the grains
287 where only one basal slip is favorable and prismatic slips are suppressed. At the same time, the
288 formed $\{11\bar{2}1\}$ twin has a quite high positive SF value. The SFs of the different plastic modes
289 in G6 are presented in Table 4. According to Table 2, K_{IR} is formed by $(0001)[11\bar{2}0]$
290 dislocation (B_1). The high SF of B_1 (0.49) is favorable for the formation of kink band, while the
291 activation of P_3 (Fig. 10a) with high SF (0.28) can locally rotate the $[1\bar{1}00]$ rotation axis of kink
292 band and restrain the nucleation of $\{11\bar{2}1\}$ twin.

293 Fig. 11a present a grain (G7) with interaction of kink band with $\{11\bar{2}2\}$ twin. According to
294 $\{11\bar{2}0\}$ pole figure in Fig. 11b, $\{11\bar{2}0\}$ plane trace is used to determine the kink band variant
295 in G7, because the plane traces of habit planes $\{11\bar{2}k\}$ parallel to $\{11\bar{2}0\}$. All the four kink
296 bands in G7 are K_2 variant with habit plane of $(1\bar{2}1k)$, formed by $(0001)[1\bar{2}10]$ (B_2) basal
297 dislocations. The two close kink bands in the middle of G7 are thicker than the other two on the
298 upper and lower sides likely due to the earlier nucleation and different local stress. Similarly to
299 G6, the nucleation of $\{11\bar{2}1\}$ twin from K_2 is restrained after large deformation due to the high
300 activity of prismatic slips, both P_1 and P_3 are observed in Fig. 11a. Specially, the kink bands
301 always connect with triple junction of grain boundaries. It can be therefore speculated that stress
302 concentration at triple junction play a favorable role on the kink band nucleation. In addition,
303 the SF of B_2 is extremely low (0.01) in Table 4, while the SFs of prismatic slips are high, P_1
304 (0.39) and P_3 (0.45). Different from G7, the SF of B_1 (0.49) in G6 is high and P_3 SF (0.28) is
305 relatively lower. The kinking deformation can be stimulated in G6 and G7 with different active
306 slip systems, thus the critical stress conditions for kink band nucleation need to be further
307 investigated.

308 Furthermore, in the yellow boxes of Fig. 4a-d, the microstructure evolution of G7 is
309 presented. With increased strain, $\{11\bar{2}2\}$ twin nucleation occurs at 16% strain and interacts with
310 pre-existing kink bands. The basal dislocation on the kink boundary in Fig. 11a corresponds to
311 perfect $\langle a \rangle$ edge dislocation and the mixed dislocations with same Burgers vector is localized
312 around kink boundary ^[15]. The growth of C_1 is hindered by the parallel kink bands with
313 complicated dislocations in G7, which shows the work hardening mechanism produced by the
314 formation of kink bands. According to Table 4, C_1 is the most favorable twin with highest SF

315 (0.40), while C_2 stimulated at the kink band boundary has negative SF (-0.01). The negative SF
 316 C_2 cannot accommodate external stress, that is induced by the accumulated dislocation and
 317 stress concentration around kink band.

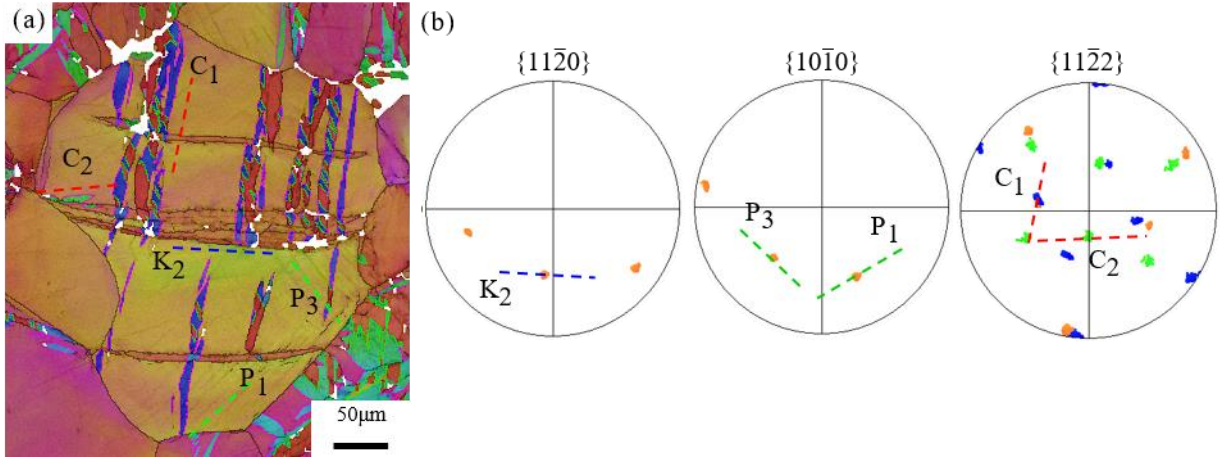


Fig. 11. (a) IPF map of G7 after 24% elongation. (b) $\{11\bar{2}0\}$, $\{10\bar{1}0\}$ and $\{11\bar{2}2\}$ pole figures. The color of dots in pole figures correspond to IPF color. The dotted lines show the traces of kink band habit plane, slip and twin plane. (Euler angle of matrix: 165.0° , 37.4° , 8.7°)

318

319 4. Discussion

320 According to the results in Section 3.1, texture evolution during tension is mainly controlled
 321 by primary $\{11\bar{2}2\}$ and secondary $\{10\bar{1}2\}$ twins. The variant selection of $\{11\bar{2}2\}$ - $\{10\bar{1}2\}$
 322 double twins in G1 (Fig. 9) is studied as an example. First, the accommodation of primary
 323 $\{11\bar{2}2\}$ twins C_5 (SF: 0.42) and C_4 (SF: 0.15) by neighboring grain is investigated by
 324 transforming the displacement gradient tensor of twinning into the crystal frame of neighboring
 325 grain [29]. The method of twinning and crystal coordinate transformation is shown in Appendix.
 326 \mathbf{D}_{g3}^{c5} refers to the displacement gradient tensors of C_5 transformed from the twin frame into G3
 327 crystal frame and \mathbf{D}_{g5}^{c4} is the displacement gradient tensors of C_4 transformed from the twin
 328 frame into G5 crystal frame, as shown in Table 5. The crystal frame of α -Ti is $x//[10\bar{1}0]$,
 329 $y//[1\bar{2}10]$ and $z//[0001]$. D_{xz} and D_{yz} represent the strain can be accommodated by single and
 330 double basal slips, D_{xy} and D_{xy} indicate the accommodation by single and double prismatic slip,
 331 the D_{zx} and D_{zy} are the accommodation by twinning.

332 According to \mathbf{D}_{g3}^{c5} , the large values of D_{xz} (0.11) and D_{yz} (0.18) show that only basal slips in
 333 G3 can accommodate the C_5 twin in G1. The basal slip is difficult slip system than prismatic
 334 slip in titanium and not enough to accommodate the shear for twin growth, and thus the size of

335 C₅ twin is limited. As for C₄, it can be accommodated by twinning in the upper grain because
 336 of the large D_{zx} (-0.13) of $\mathbf{D}_{g_5}^{c_4}$. Indeed, obvious twin interaction between them can be observed
 337 in Fig. 7c and the interaction is more significant in Fig. 9d. The $\mathbf{D}_{g_5}^{c_4}$ is transformed into the
 338 twinning frame of activated $\{11\bar{2}2\}$ twin (C₄) in G5 ($\mathbf{D}_{c_1}^{c_4}$) using the method in Appendix. The
 339 resulting tensor $\mathbf{D}_{c_1}^{c_4}$ is shown in Table 5 and has a large positive D_{13} (0.19), which means the
 340 twin in G5 can accommodate the shear of C₄. Thus, the twin with lower SF can be more stable
 341 when it can be accommodated by the twin in the neighbor grain. However, the volume fraction
 342 of twin variants showing such a non-Schmid behavior is limited in the whole sample, the SF
 343 criterion is a major mechanism controlling twinning [10].

344 C₄-T₅ is the dominant double twin in G1. Indeed, the formed $\{11\bar{2}2\}$ - $\{10\bar{1}2\}$ double twins
 345 in α -Ti always follow the C_i-T_i/T_{i+1} group proposed by Xu et al. [30]. The T_i/T_{i+1} variants are
 346 activated to accommodate the local shear of primary C_i twin. To further investigate the variant
 347 selection between T_i and T_{i+1} variant, the accommodation capacity on C_i twinning is compared
 348 by transforming the \mathbf{D}^t of all the C₄, T₄ and T₅ into the crystal frame of C₄. The results are
 349 shown in Table 5. Compared with $\mathbf{D}_{g(c_4)}^{t_4}$, all the nine components of $\mathbf{D}_{g(c_4)}^{t_5}$ tensor are non-zero
 350 and the same sign with $\mathbf{D}_{g(c_4)}^{c_4}$. It means that T₅ can more effectively accommodate the local
 351 strain of C₄ along all the crystal directions than T₄. To verify the above result, all the double
 352 twins in Fig. 4d are determined, 64.4% (area fraction) of secondary $\{10\bar{1}2\}$ twins belongs to
 353 the group C_i-T_{i+1}, which is a little smaller than the twin fraction respecting the SF rule, 70.8%
 354 twin with NSF ≥ 0.9 (Fig. 8). According to Fig. 7c, the basal poles of primary $\{11\bar{2}2\}$ twins
 355 oriented along **TD** after 24% tension, thus the NSF values of six secondary $\{10\bar{1}2\}$ variants are
 356 always similar and larger than 0.9. However, C_i-T_{i+1} group can more efficiently determine the
 357 most favorable variant T_{i+1}.

358 According to the above analysis, to predict the texture evolution induced by $\{11\bar{2}2\}$ - $\{10\bar{1}2\}$
 359 double twins, the activation of primary $\{11\bar{2}2\}$ twin is determined by SF criterion and the
 360 selected secondary $\{10\bar{1}2\}$ twin follows C_i-T_{i+1}. The $\{0001\}$ pole figure of initial sample in Fig.
 361 4e shows the split basal texture with *c*-axis oriented from **ND** to **TD** and the *a*-axis is random.
 362 The Euler angles of initial grain orientations are set as [90°, 30°, 0-10° & 50-60°] (right basal
 363 poles) and [270°, 30°, 180-190° & 230-240°] (left basal poles). The initial orientations of [90°,
 364 30°, 10-50°] and [270°, 30°, 190-230°] with the SFs of primary $\{11\bar{2}2\}$ twins less than 0.4 are
 365 excluded. The basal pole locations of selected primary $\{11\bar{2}2\}$ and secondary $\{10\bar{1}2\}$ twins are
 366 calculated and projected into pole figure (see Fig. 12). The basal poles of primary $\{11\bar{2}2\}$ twins

367 (blue) are less than 10° oriented from **TD** and the basal poles of secondary $\{10\bar{1}2\}$ twins (red)
 368 are oriented around 20° from **ND** to **RD**. The prediction is consistent to the Fig. 7a. The weak
 369 peak at C_4 position (Fig. 7c) and strong peak at T_5 position (Fig. 7d) shows the main double
 370 twin in the observed area of 24% elongation sample is C_4 - T_5 .

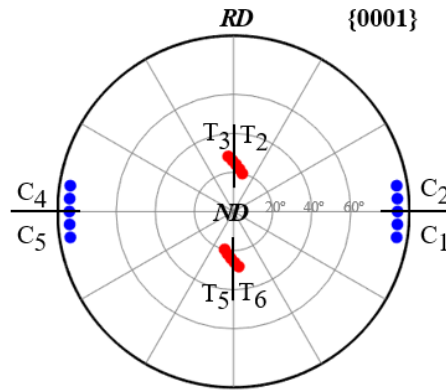


Fig. 12. The basal pole location of primary $\{11\bar{2}2\}$ twin (C_i) with $SF > 0.4$ and corresponding secondary $\{10\bar{1}2\}$ twin (T_{i+1})

371 5. Conclusion

372 In this work, interrupted in-situ tension was performed to investigate the microstructure
 373 evolution of commercial pure titanium during plastic deformation.

374 $\{11\bar{2}2\}$ compression and $\{10\bar{1}2\}$ tension twins are dominant twin modes on the observed
 375 surface after 8%, 16% and 24% elongation along **TD**. The anisotropic activation of deformation
 376 twin, especially $\{11\bar{2}2\}$ - $\{10\bar{1}2\}$ double twin, is the reason for the texture evolution during
 377 deformation. The primary $\{11\bar{2}2\}$ twin is responsible for the aligned basal poles along **TD** and
 378 the secondary $\{10\bar{1}2\}$ twin reoriented the basal poles parallel to **ND**. Although some non-
 379 Schmid twins are induced by local stress concentration, more than 60% deformation twins
 380 respect SF criterion. To predict the texture evolution produced by $\{11\bar{2}2\}$ - $\{10\bar{1}2\}$ double twin,
 381 the primary $\{11\bar{2}2\}$ variant followed SF rule and the variant selection of secondary $\{10\bar{1}2\}$
 382 twin was determined by DGA.

383 Interestingly, kink bands formed by the accumulation of basal $\langle a \rangle$ dislocations were
 384 observed. The kink band variant were determined by the trace of habit plane $\{11\bar{2}k\}$. The
 385 activation of other slip systems, for example prismatic $\langle a \rangle$ slips, can deviate the rotation axis
 386 and reduce the rotation angle of kink boundary. Besides, twin growth extremely hindered by
 387 kink boundary is responsible for the hardening behavior of CP-Ti at large strain.

389 **Acknowledgements**

390 The first author Qian Wang is grateful to the China Scholarship Council for the support of
391 her Ph.D. study in France.

392

393 **References**

- 394 1 M. Ishiki, T. Kuwabara, and Y. Hayashida: *Int. J. Mater. Form.*, 2011, vol. 4, pp. 193–204.
395 2 Z. Zeng, Y. Zhang, and S. Jonsson: *Mater. Des.*, 2009, vol. 30, pp. 3105–11.
396 3 Y.B. Chun, S.H. Yu, S.L. Semiatin, and S.K. Hwang: *Mater. Sci. Eng. A*, 2005, vol. 398, pp. 209–19.
397 4 N.P. Gurao, R. Kapoor, and S. Suwas: *Acta Mater.*, 2011, vol. 59, pp. 3431–46.
398 5 M. Battaini, E. V Pereloma, and C.H.J. Davies: *Metall. Mater. Trans. A*, 2007, vol. 38, pp. 276–85.
399 6 S. Panda, S.K. Sahoo, A. Dash, M. Bagwan, G. Kumar, S.C. Mishra, and S. Suwas: *Mater. Charact.*,
400 2014, vol. 98, pp. 93–101.
401 7 X. Huang, K. Suzuki, and Y. Chino: *Scr. Mater.*, 2010, vol. 63, pp. 473–6.
402 8 M.H. Yoo: *Metall. Trans. A*, 1981, vol. 12, pp. 409–18.
403 9 Y. Ren, X. Zhang, T. Xia, Q. Sun, and Q. Liu: *Mater. Des.*, 2017, vol. 126, pp. 123–34.
404 10 J.W. Won, D. Kim, S.G. Hong, and C.S. Lee: *J. Alloys Compd.*, 2016, vol. 683, pp. 92–9.
405 11 S. Wang, C. Schuman, L. Bao, J.S. Lecomte, Y. Zhang, J.M. Raulot, M.J. Philippe, X. Zhao, and C.
406 Esling: *Acta Mater.*, 2012, vol. 60, pp. 3912–9.
407 12 S. Xu, M. Gong, Y. Jiang, C. Schuman, J.S. Lecomte, and J. Wang: *Acta Mater.*, 2018, vol. 152, pp. 58–
408 76.
409 13 J.B. Hess and C.S. Barrett: *JOM*, 1949, vol. 1, pp. 599–606.
410 14 K. Hagihara, T. Mayama, M. Honnami, M. Yamasaki, H. Izuno, T. Okamoto, T. Ohashi, T. Nakano, and
411 Y. Kawamura: *Int. J. Plast.*, 2016, vol. 77, pp. 174–91.
412 15 T. Matsumoto, M. Yamasaki, K. Hagihara, and Y. Kawamura: *Acta Mater.*, 2018, vol. 151, pp. 112–24.
413 16 S. Yamasaki, T. Tokuzumi, W. Li, M. Mitsuhara, K. Hagihara, T. Fujii, and H. Nakashima: *Acta Mater.*
414 17 S. Jin, K. Marthinsen, and Y. Li: *Acta Mater.*, 2016, vol. 120, pp. 403–14.
415 18 M. Yamasaki, K. Hagihara, S.I. Inoue, J.P. Hadorn, and Y. Kawamura: *Acta Mater.*, 2013, vol. 61, pp.
416 2065–76.
417 19 N.J. Lane, S.I. Simak, A.S. Mikhaylushkin, I.A. Abrikosov, L. Hultman, and M.W. Barsoum: *Phys. Rev.*
418 *B*, 2011, vol. 84, p. 184101.
419 20 Y. Zheng, W. Zeng, Y. Wang, and S. Zhang: *Mater. Sci. Eng. A*, 2017, vol. 702, pp. 218–24.
420 21 S. Wronski, M. Jedrychowski, J. Tarasiuk, and B. Bacroix: *Mater. Sci. Eng. A*, 2017, vol. 692, pp. 113–
421 26.
422 22 S. Wang, Y. Zhang, C. Schuman, J.S. Lecomte, X. Zhao, L. Zuo, M.J. Philippe, and C. Esling: *Acta*
423 *Mater.*, 2015, vol. 82, pp. 424–36.
424 23 B. Beausir and J.-J. Fundenberger: *Analysis Tools for Electron and X-Ray Diffraction, ATEX - Software,*
425 *Université de Lorraine - Metz*, 2017.
426 24 W. Pantleon: *Scr. Mater.*, 2008, vol. 58, pp. 994–7.
427 25 É. Martin, L. Capolungo, L. Jiang, and J.J. Jonas: *Acta Mater.*, 2010, vol. 58, pp. 3970–83.
428 26 Y.B. Chun, M. Battaini, C.H.J. Davies, and S.K. Hwang: *Metall. Mater. Trans. A*, 2010, vol. 41, pp.
429 3473–87.
430 27 S. Xu, L.S. Toth, C. Schuman, J.-S. Lecomte, and M.R. Barnett: *Acta Mater.*, 2017, vol. 124, pp. 59–70.
431 28 T. Hama, A. Kobuki, and H. Takuda: *Int. J. Plast.*, 2017, vol. 91, pp. 77–108.
432 29 J.J. Jonas, S. Mu, T. Al-Samman, G. Gottstein, L. Jiang, and É. Martin: *Acta Mater.*, 2011, vol. 59, pp.
433 2046–56.
434 30 S. Xu, M. Gong, C. Schuman, J.-S. Lecomte, X. Xie, and J. Wang: *Acta Mater.*, 2017, vol. 132, pp. 57–
435 68.
436 31 A. Ghaderi and M.R. Barnett: *Acta Mater.*, 2011, vol. 59, pp. 7824–39.

437

438

439 **Appendix**

440 To investigate the accommodation mechanism, the displacement gradient tensor of twinning \mathbf{D}^t is always
 441 transformed into other coordinate system, such as crystal system, sample system or another twinning system. First,
 442 we need to build the coordinate rotation matrix from twinning system to crystal system.

$$\mathbf{R}_{tg} = \begin{bmatrix} n_1 & n_2 & n_3 \\ p_1 & p_2 & p_3 \\ m_1 & m_2 & m_3 \end{bmatrix} \quad (\text{A1})$$

443 where \mathbf{n} , \mathbf{m} and \mathbf{p} represent the twinning shear direction (\mathbf{n}), normal of twin habit plane (\mathbf{m}) and normal of shear
 444 plane (\mathbf{p}). The coordinate rotation matrix sample system to crystal system is:

445 $\mathbf{R}_{gs} = \mathbf{R}_{\varphi_2} \cdot \mathbf{R}_{\Phi} \cdot \mathbf{R}_{\varphi_1}$

$$\mathbf{R}_{\varphi_1} = \begin{bmatrix} \cos\varphi_1 & \sin\varphi_1 & 0 \\ -\sin\varphi_1 & \cos\varphi_1 & 0 \\ 0 & 0 & 1 \end{bmatrix} \quad (\text{A2})$$

$$\mathbf{R}_{\Phi} = \begin{bmatrix} 1 & 0 & 0 \\ 0 & \cos\Phi & \sin\Phi \\ 0 & -\sin\Phi & \cos\Phi \end{bmatrix} \quad (\text{A3})$$

$$\mathbf{R}_{\varphi_2} = \begin{bmatrix} \cos\varphi_2 & \sin\varphi_2 & 0 \\ -\sin\varphi_2 & \cos\varphi_2 & 0 \\ 0 & 0 & 1 \end{bmatrix} \quad (\text{A4})$$

446 where φ_1 , Φ and φ_2 are Euler angles from HKL system. The displacement gradient tensor of Twin 1 (\mathbf{D}^{t1}) is
 447 transformed from Twin 1 frame (\mathbf{D}_{t1}^{t1}) to crystal frame of Grain 1 (\mathbf{D}_{g1}^{t1}) as follows:

$$\mathbf{D}_{g1}^{t1} = \mathbf{R}_{t1g1}^{-1} \cdot \mathbf{D}_{t1}^{t1} \cdot \mathbf{R}_{t1g1} \quad (\text{A5})$$

448 The transformation of \mathbf{D}^{t1} from Grain 1 frame (\mathbf{D}_{g1}^{t1}) to sample frame (\mathbf{D}_s^{t1}) to Grain 2 frame (\mathbf{D}_{g2}^{t1}) is:

$$\mathbf{D}_{g2}^{t1} = \mathbf{R}_{g2s} \cdot \mathbf{D}_s^{t1} \cdot \mathbf{R}_{g2s}^{-1} = \mathbf{R}_{g2s} \cdot \mathbf{R}_{g1s}^{-1} \cdot \mathbf{D}_{g1}^{t1} \cdot \mathbf{R}_{g1s} \cdot \mathbf{R}_{g2s}^{-1} \quad (\text{A6})$$

449 The transformation of \mathbf{D}^{t1} from Grain 2 frame (\mathbf{D}_{g2}^{t1}) to the frame (\mathbf{D}_{t2}^{t1}) of Twin 2 in Grain 2 is:

$$\mathbf{D}_{t2}^{t1} = \mathbf{R}_{t2g2} \cdot \mathbf{D}_{g2}^{t1} \cdot \mathbf{R}_{t2g2}^{-1} \quad (\text{A7})$$

450